



Quantitative optical mapping of two-dimensional materials

Jessen, Bjarke S.; Whelan, Patrick R.; Mackenzie, David M. A.; Luo, Birong; Thomsen, Joachim D.; Gammelgaard, Lene; Booth, Timothy J.; Bøggild, Peter

Published in:
Scientific Reports

Link to article, DOI:
[10.1038/s41598-018-23922-1](https://doi.org/10.1038/s41598-018-23922-1)

Publication date:
2018

Document Version
Publisher's PDF, also known as Version of record

[Link back to DTU Orbit](#)

Citation (APA):
Jessen, B. S., Whelan, P. R., Mackenzie, D. M. A., Luo, B., Thomsen, J. D., Gammelgaard, L., Booth, T. J., & Bøggild, P. (2018). Quantitative optical mapping of two-dimensional materials. *Scientific Reports*, 8(1), [6381]. <https://doi.org/10.1038/s41598-018-23922-1>

General rights

Copyright and moral rights for the publications made accessible in the public portal are retained by the authors and/or other copyright owners and it is a condition of accessing publications that users recognise and abide by the legal requirements associated with these rights.

- Users may download and print one copy of any publication from the public portal for the purpose of private study or research.
- You may not further distribute the material or use it for any profit-making activity or commercial gain
- You may freely distribute the URL identifying the publication in the public portal

If you believe that this document breaches copyright please contact us providing details, and we will remove access to the work immediately and investigate your claim.

SCIENTIFIC REPORTS

OPEN

Quantitative optical mapping of two-dimensional materials

Bjarke S. Jessen^{1,2}, Patrick R. Whelan², David M. A. Mackenzie^{1,2}, Birong Luo², Joachim D. Thomsen², Lene Gammelgaard², Timothy J. Booth^{1,2} & Peter Bøggild^{1,2}

Received: 12 December 2017

Accepted: 23 March 2018

Published online: 23 April 2018

The pace of two-dimensional materials (2DM) research has been greatly accelerated by the ability to identify exfoliated thicknesses down to a monolayer from their optical contrast. Since this process requires time-consuming and error-prone manual assignment to avoid false-positives from image features with similar contrast, efforts towards fast and reliable automated assignments schemes is essential. We show that by modelling the expected 2DM contrast in digitally captured images, we can automatically identify candidate regions of 2DM. More importantly, we show a computationally-light machine vision strategy for eliminating false-positives from this set of 2DM candidates through the combined use of binary thresholding, opening and closing filters, and shape-analysis from edge detection. Calculation of data pyramids for arbitrarily high-resolution optical coverage maps of two-dimensional materials produced in this way allows the real-time presentation and processing of this image data in a zoomable interface, enabling large datasets to be explored and analysed with ease. The result is that a standard optical microscope with CCD camera can be used as an analysis tool able to accurately determine the coverage, residue/contamination concentration, and layer number for a wide range of presented 2DMs.

The discovery that atomically thin two-dimensional (2D) materials could be visualised optically has arguably been the single most important enabler for the explosive emergence of 2D materials research¹. On suitable substrates, such as thin SiO₂ on Si, the optical contrast of, e.g. single-layer graphene can be as high as 14%, which enables the identification of individual layers using standard white-light microscopy. Optical microscopy - while still used to hunt down individual monolayers of mechanically exfoliated 2D crystals for fundamental research and prototyping² - is now also a crucial tool for process development inspection and quality control within large-area graphene growth and transfer processes^{3–5}.

Despite remarkable progress in the quality of both growth^{6–11} and transfer^{3–5,12,13} of 2D materials, the atomic thinness and high surface area-to-volume ratio of these materials make them exceptionally susceptible to non-uniformities such as contamination, atomic and mechanical defects, and secondary layer growth, which in turn is reflected in key performance metrics¹⁴ such as electrical conductivity¹⁵, charge carrier mobility¹⁶, and barrier properties¹⁷. Understanding the origin of such variations and monitoring their effect is critical for quality control and R&D alike. While the human eye is naturally fine-tuned at “change detection”¹⁸, machine vision is needed to meet the requirements of automated, quantitative, reliable, and high-throughput low-cost inspection. For achieving the highest possible reliability in identification and analysis of chemical vapour deposited (CVD) films and exfoliated two-dimensional materials, it is necessary that both false-positives and false-negatives are avoided.

Here we show that accurate estimates for the pixel contrasts of 2D materials can be modelled in the well-known framework of multiple Fresnel reflections, and then used as a starting point for consistent identification of 2D crystals. To reduce false-positives and false-negatives as far as possible the individual RGB (Red, Green, Blue) spectral profiles of the light source, the 2D material-SiO₂ interface, and finally the charge-coupled device (CCD) camera are taken into account. We then present a robust methodology for reliably discriminating between 2D material flakes or films and other confounding image elements with similar contrast, such as resist residues and other contaminants. Coverage is a *de-facto* standard for characterising the quality of graphene growth and transfer, and the approach presented here provides a fast, reliable, and quantitative means of obtaining the actual

¹Center for Nanostructured Graphene (CNG), Technical University of Denmark, DK-2800, Kgs. Lyngby, Denmark.

²Department of Micro- and Nanotechnology (DTU Nanotech), Technical University of Denmark, DK-2800, Kgs. Lyngby, Denmark. Bjarke S. Jessen and Patrick R. Whelan contributed equally to this work. Correspondence and requests for materials should be addressed to B.S.J. (email: bjarke.jessen@nanotech.dtu.dk) or P.B. (email: peter.boggild@nanotech.dtu.dk)

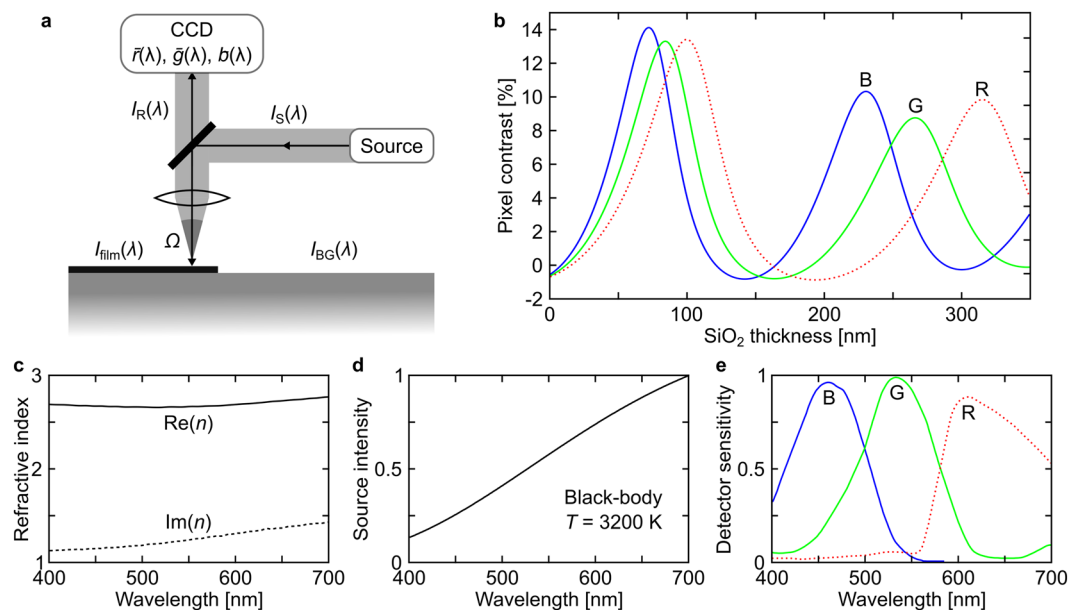


Figure 1. (a) Illustration of a typical optical setup where light from a source with spectral intensity $I_S(\lambda)$ interacts with the substrate and optical components and arrives at a detector as $I_R(\lambda)$. $I_{\text{film}}(\lambda)$ and $I_{\text{BG}}(\lambda)$ are the reflected spectral intensities from the material to be identified and the background, respectively. (b) Calculated red, green and blue pixel contrast of single-layer graphene on a SiO_2/Si substrate as a function of varying thickness of SiO_2 . (c,d,e) Wavelength-dependent input to the contrast calculations. (c) Real and imaginary part of the refractive index of graphene. (d) Typical intensity characteristics of an incandescent light-source. (e) Spectral sensitivity of a Sony ICX282AQ CCD camera.

coverage of transferred graphene. Finally, we demonstrate how arbitrarily large datasets can be processed for easy inspection and analysis, which greatly improves the practicality of our approach, thereby providing a fast, reliable, and highly accurate means of obtaining the numerical coverage, a quantitative indicator of the quality (e.g. coverage percentage, layer number, contamination density) of transferred CVD-based 2D material films, for arbitrarily large samples.

Materials and Methods

Growth and Exfoliation. CVD graphene was grown on electropolished copper foils using a commercially available Black Magic Pro CVD system. The growth recipe is based on a published recipe¹⁹ with an annealing phase in H_2/Ar where CH_4 was added as a precursor for the growth phase at 1000°C followed by a cool down in Ar. Graphene was transferred from the copper foil to 90 nm SiO_2 using either a standard wet etching process^{20,21} or the electrochemical oxidative decoupling transfer method³. Exfoliated graphene and WSe_2 samples were made by the standard “Scotch tape” technique²², using low-contamination SWT 10+ tape from Nitto Denko.

Optical Characterization. Optical microscopy was conducted with a Nikon Eclipse L200N, equipped with a programmable Prior Scientific XYZ stage and a Nikon DS-Fi2 camera (Sony ICX282AQ CCD).

Raman spectroscopy was performed with a Thermo Fisher DXRxi spectrometer equipped with a 532 nm excitation laser source using 1 mW laser power and 100x objective. We use the intensity ratio of the graphene 2D and G Raman peaks determined from fits to single Lorentzian functions²³ to distinguish between single and bilayer graphene on SiO_2 . The $I(2\text{D})/I(\text{G})$ peak intensity ratio is set to 0 in pixels where there is no detectable Raman G peak.

Results and Discussion

Calculating Pixel Contrast. Detection of 2D materials in white-light microscopy, whether by eye or machine vision techniques, relies on a detectable difference in the intensity of reflected light from the target material and its substrate, which depends on the path of light in the optical setup. A generic schematic of machine vision or optical inspection of 2D materials in the visible regime is shown in Fig. 1(a). Here the sample, a substrate covered with 2D material regions of different lateral sizes and thicknesses in addition to a range of other particles and contamination is illuminated by a light-source with spectral intensity $I_S(\lambda)$. The reflected light from the sample, either $I_{\text{BG}}(\lambda)$ from the reference background or $I_{\text{film}}(\lambda)$ from the 2D material, is collected and focused by lenses onto a detector, which finally converts the light to red, green, and blue digital pixel intensities according to its spectral sensitivity functions $\bar{r}(\lambda)$, $\bar{g}(\lambda)$, and $\bar{b}(\lambda)$, respectively. 2D materials are commonly identified from their wavelength-dependant optical contrast, $C(\lambda) = (I_{\text{BG}}(\lambda) - I_{\text{film}}(\lambda))/I_{\text{BG}}(\lambda)$. In order to identify the presence of a given 2D material the corresponding pixel values of digitally captured images must be identified during inspection. To this end, the spectral intensities are substituted with the calculated or digitally captured pixel

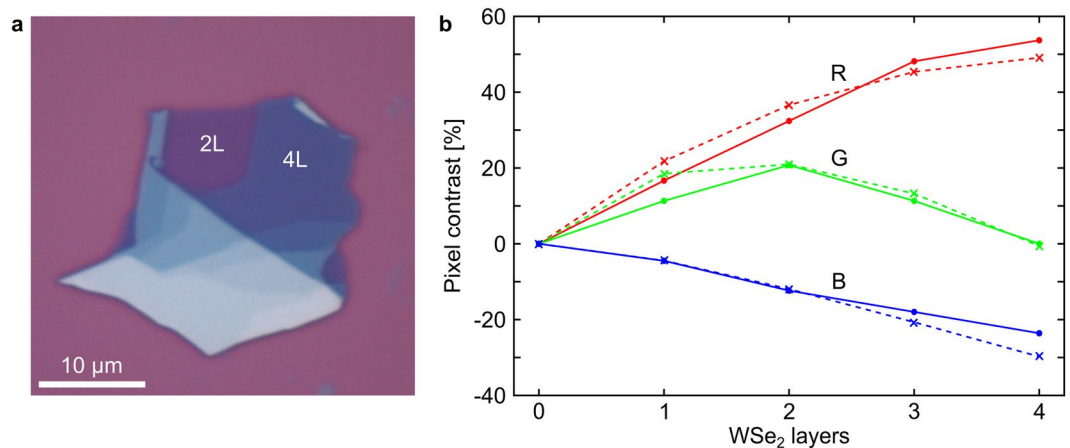


Figure 2. (a) Optical image of exfoliated WSe₂ crystal with different number of layers on 300 nm SiO₂. (b) Contrast of WSe₂ as a function of number of layers on 300 nm SiO₂. Crosses are calculated contrasts based on the wavelength dependent refractive index of WSe₂. Dots are extracted from digital optical images with red, green and blue channels giving three separate values of contrasts for each thickness.

intensities. With a given light-source, reflection spectrum, and camera spectral sensitivity function, the absolute intensities of RGB pixels are given by

$$R = \int_0^\infty I_R(\lambda) I_S(\lambda) \bar{r}(\lambda) d\lambda, \quad (1a)$$

$$G = \int_0^\infty I_R(\lambda) I_S(\lambda) \bar{g}(\lambda) d\lambda, \quad (1b)$$

$$B = \int_0^\infty I_R(\lambda) I_S(\lambda) \bar{b}(\lambda) d\lambda, \quad (1c)$$

where $I_R(\lambda)$ is the spectral intensity of light reaching the detector, either from the background, $I_{BG}(\lambda)$, or from the 2D material, $I_{film}(\lambda)$. The reflection spectra are functions of the thickness and refractive indices of the given material stack, along with the angular distribution of the impinging light²⁴. The details of calculating the reflection spectra can be involved^{25–28}, and should for critical applications include the effect of lenses and other optical elements in the specific setup. In this work, we restrict ourselves to thin-film calculations for normal incident light similar to previous work by Blake *et al.*¹. Contrast calculations for non-normal incident light, in particular describing discrepancies between observed and expected contrast due to high numerical aperture objectives can be seen in the Supplementary Information.

With a given material and its refractive index, along with illumination and camera characteristics, the pixel intensities for, *e.g.* graphene and its substrate can now be calculated and used to obtain a set of (pixel) contrast curves, as shown in Fig. 1(b). Here, we have used the ellipsometrically measured refractive index of single-layer graphene, Si, and SiO₂^{29–31}, the intensity profile of an incandescent light source (3200 K black-body spectrum) and a typical CCD response function (see methods) as shown in Fig. 1(c–e), which yields quantitative values of the contrast of 2D materials in digital optical images. As is well known¹, the optimal thickness of SiO₂ for simultaneous high contrast across the visible spectrum is 90 nm. Similarly, we find the highest RGB pixel contrasts for 90 nm SiO₂, where the green contrast is slightly higher than the red and blue contrasts, which is opportune for manual identification, due to the high sensitivity of the human eye to green light³². These contrast values then serve as the starting point for a machine vision approach to identify the presence of 2D materials in digital images. Any color shift introduced by the optical path of the imaging system will affect all images uniformly, and will not affect contrasts so as to cause misidentification of layer number (in effect a contrast inversion) in any well designed system. Through manual calibration such as white balancing small color shifts can also be well accounted for.

There is a lack of data and consensus on the layer-number dependent values of the optical constants of other 2D materials, such as most of the transition metal dichalcogenides, in particular where changes in these constants associated with the transition from indirect to direct bandgap structures are expected for the monolayer. We note however that for published systems such as WSe₂ the assumption that the optical constants do not change from bulk to monolayer is not coarse enough to cause a misidentification of the monolayer as a bilayer, and can therefore be applied in these cases. Figure 2 shows the pixel contrasts extracted from optical images of exfoliated WSe₂ compared to values calculated from the wavelength dependent refractive index of bulk WSe₂³³, and a comparison between pixel contrasts obtained with monolayer and bulk refractive indices can be found in the Supplementary Information.

The experimentally and theoretically determined contrasts are in good agreement despite changes in the electronic band structure when going from single to few-layer WSe₂³⁴. This shows that the expected RGB contrast can be successfully calculated for a wider range of 2D materials with varying thickness than simply graphene (Fig. 1) and hexagonal boron nitride (hBN)^{2,4,35,36}. We caution that the assumption of bulk optical constants for

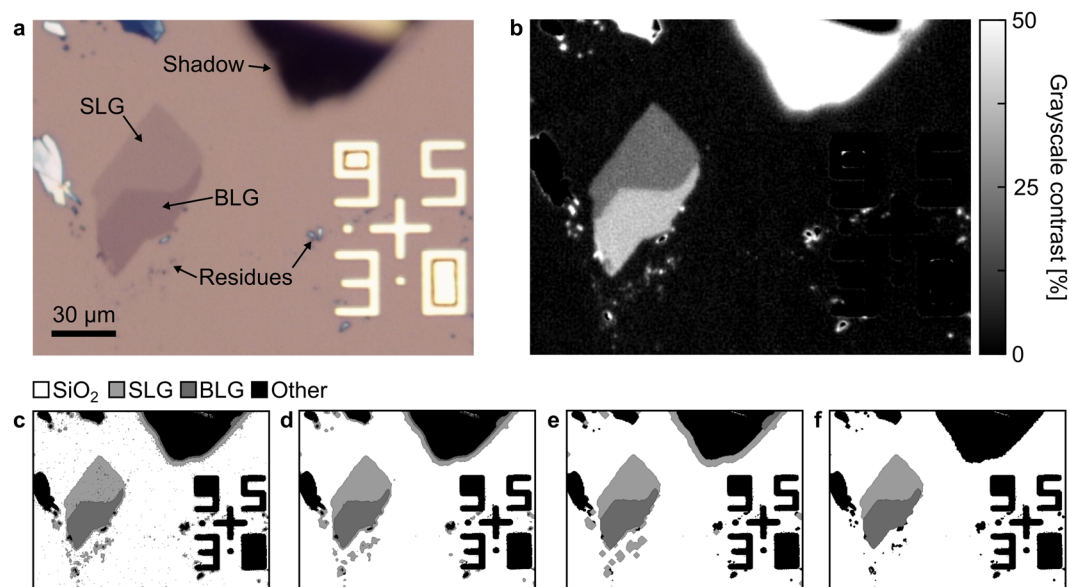


Figure 3. (a) Optical image of exfoliated graphene on 300 nm SiO_2 . The sample contains typical features of an optical image of an exfoliated sample, such as single- and bi-layer graphene, graphite, and residues, a shadow from bulk graphite, and optical alignment marks. (b) Map of the positive grey-scale contrasts in the image. (c) Segmented image where every pixel has been categorized either as SLG, BLG, SiO_2 , or other, using only the expected contrast values. (d) Segmented image after edge-preserving median filtering, and (e) after erode and dilate filtering. (f) Segmented image after contour filtering, resulting in a >99% pixel-for-pixel correspondence between expected and automatically detected pixels.

monolayers of a given material is not likely to be universally accurate, and must be tested for validity for new materials accordingly.

Quantitative Identification. Once the expected contrast of a 2D material on a given substrate is known, it is in principle possible to select the corresponding pixels of a digital image, thus identifying regions where any 2D materials are located. Figure 3(a) shows a typical optical image of exfoliated graphene on SiO_2 which we use to illustrate the effect of the individual steps of our method. The image contains several different visible elements: a region of single-layer graphene (SLG), bi-layer graphene (BLG), alignment marks in gold, residues (tape adhesive and graphitic fragments), and a shadow from a nearby folded graphite flake. While the presence of SLG is immediately visible by optical inspection, many other regions of the area show contrast close to the expected contrast of single-layer graphene. This is evident from the corresponding map of the grey-scale contrast, Fig. 3(b), where the graphite shadow and residues have similar grey-scale contrast as the single-layer graphene, relative to the substrate, and therefore could be easily confused if a grey-scale analysis was used.

Grey-scale images, sometimes converted from RGB images³⁷, can be used to identify 2D materials^{26,38,39}. However, since RGB images retain a degree of spectral information, significantly better results can be achieved by individually treating each RGB channel⁴⁰. This is especially evident for materials such as hBN where the contrast changes sign over the visible optical range², and therefore the grey-scale contrast can be zero even when the individual RGB contrasts are not.

By filtering the image based on a certain range of RGB contrasts around the value expected for the different 2D materials and layer thicknesses to be identified, we arrive at an image with clear regions of SLG, BLG and SiO_2 , as seen in Fig. 3(c), where any remaining pixels are designated as “other”. While outlining most of the SLG and BLG, the image still reveals numerous missing pixels in the interior of the graphene flakes and false-positives from the surrounding residues and graphite shadow^{40–42}.

First, we apply a median filter to the image, as seen in Fig. 3(d). This effectively removes impulse noise while keeping edges sharp^{43,44}. With the impulse noise removed, the full interior of the SLG and BLG can be identified.

Next, we apply consecutive erode and dilate filters, as seen in Fig. 3(e). Erode and dilate, from mathematical morphology, effectively removes or adds pixels around a shape in binary images⁴⁵. By applying these filters consecutively, small and thin features, such as small particles, tape residues, and other contamination, are completely removed by the first erode filter, while larger structures are mostly preserved by the subsequent dilate filter. This effectively removes the smallest of the false-positive features but does slightly soften sharp features such as corners. It should be noted, however, the dilate and erode filters can have the effect of smoothing out sharp features such as corners, as seen in Fig. 3(e), and is further discussed in the Supplementary Information. This slight softening is preferable to returning a large number of few-pixel sized false positives since the structure of sharp corners can be effectively reconstructed by polygonal contour fitting of the shape boundary in later steps, the processing overhead relating to large numbers of false positives is eliminated and that very small areas of material are typically of limited technological interest or not the material of interest.

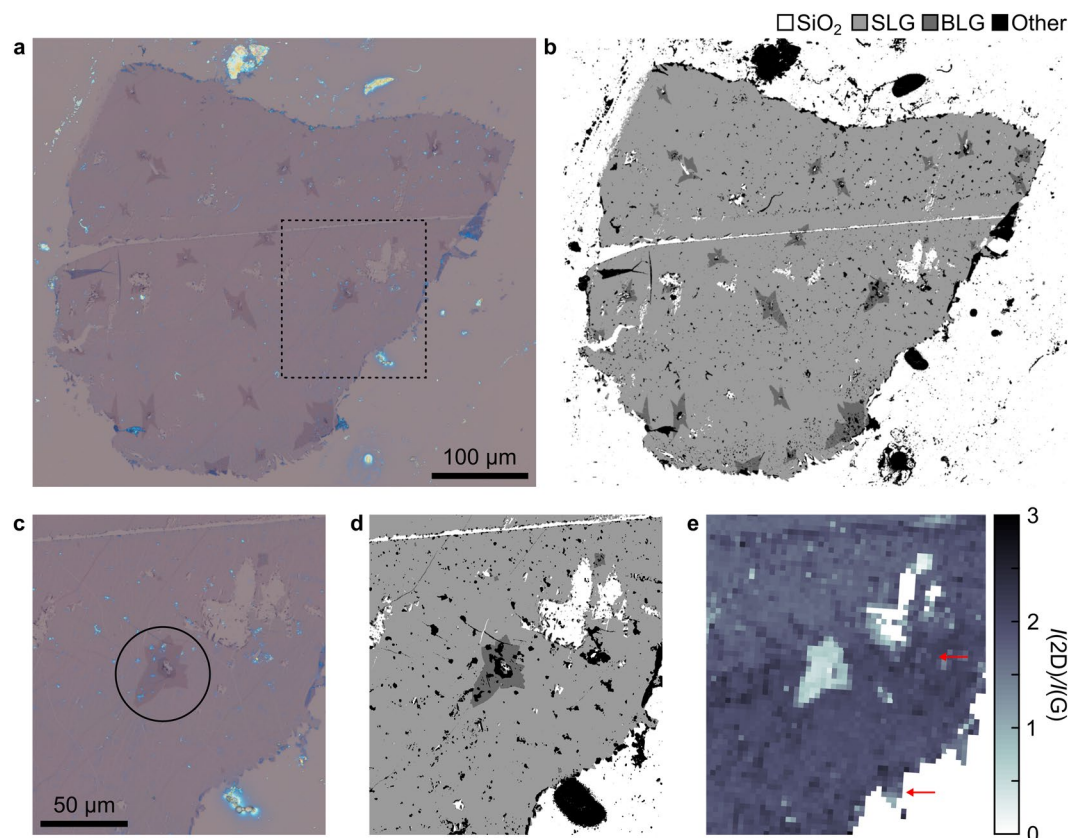


Figure 4. Comparison between optical, coverage and Raman maps of CVD graphene transferred by wet etching to 90 nm SiO₂. (a) Optical map of graphene consisting of several images stitched together. (b) Coverage map of the sample in (a) with colour codes for SiO₂, SLG, BLG, and other. (c) Zoom-in on the area inside the dotted square in (a) with the corresponding coverage map in (d) showing the detail level of the optical and coverage maps. The circle in (a) highlights an area with BLG surrounding a small region with three layer graphene and SiO₂. (e) Raman map of the $I(2D)/I(G)$ peak intensity ratio for the area shown in (c) and (d).

Finally, we add an edge-detection algorithm to mark up all identified regions by their polygon-approximated contour outlines⁴⁶. Each identified contour is now represented by n -sided polygons, described by a list of n pixels around the perimeter. From these contours, a range of shape-dependent quantities can be directly extracted, such as area and perimeter; and quantities such as circularity, pseudo-width, and pseudo-length can be derived from these. These quantities can now be used as a final filtering criterion, such as filtering out remaining small-area particles from their contour-area, or eliminating shadows from graphite pieces due to their crescent-shape leading to a low contour-circularity. As for the edge-detection, the previous removal of noise and false-positives strongly decreases the computation time for the contour-filtering, which is only needed on a small number of items. This procedure results in a highly reliable identification, as seen in Fig. 3(f), with a low computational cost. Furthermore, all of the steps described can be implemented with well-documented algorithms from highly optimised image processing libraries, making identification of 2D materials straightforward to implement, high-throughput, and scalable.

Large-scale coverage analysis. To demonstrate large-scale coverage analysis, which is an important aspect of 2D materials quality-control, a transferred CVD graphene sample was imaged with the quantitative optical method described above and compared with spatial maps of relevant micro-Raman spectroscopic parameters. The sample was grown on Cu foil and transferred to SiO₂ by wet etching (see Methods) and exhibits a certain fraction of macroscopic defects, bi-layer areas (either folded or secondary growth), and contamination predominantly from polymer residues.

Large-area optical maps of the graphene were generated by stitching together the acquired images, Fig. 4(a). Quantitative coverage analysis was used to identify regions of SLG and BLG, which are shown in Fig. 4(b) as light grey and dark grey pixels, respectively. Pixels with zero contrast can be ascribed to SiO₂, and are shown as white pixels. Finally, pixels categorised as “other” fall outside any of the other categories, and represent areas with three graphene layers or more, as well as areas contaminated by polymer residues or other remnants from the growth and transfer processes. The resulting coverage map is shown in Fig. 4(b) and highlights contamination and defects in the transfer which might otherwise not be clearly visible. The coverage can subsequently be calculated as the fraction of pixels identified as graphene and the total number of pixels in a defined region of the sample. For the sample shown in Fig. 4(b) the coverage of SLG is 48.6%, BLG 2.6%, and “other” is 6.8%.

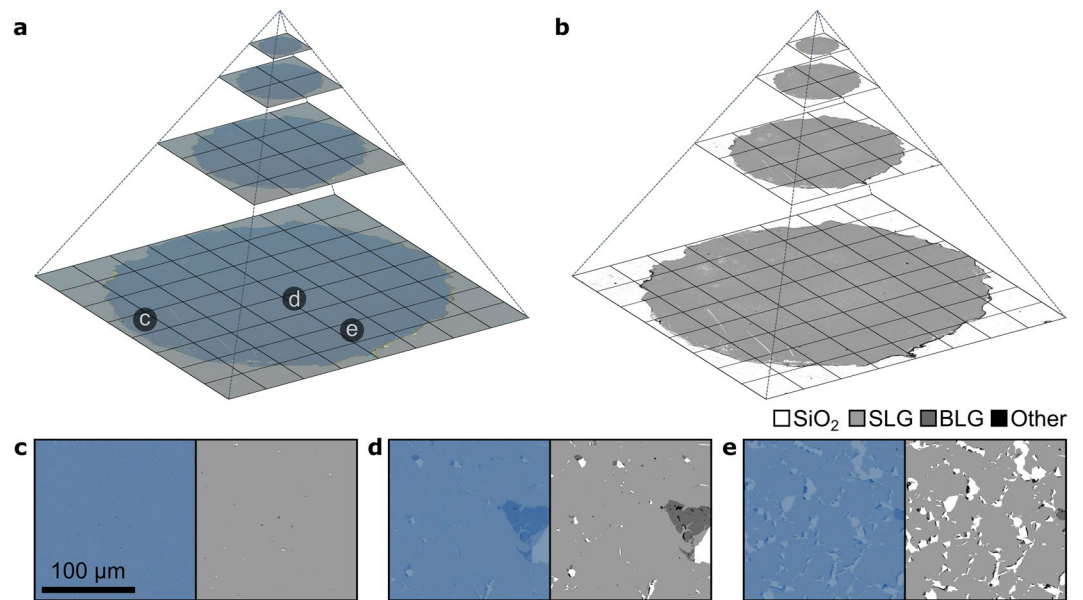


Figure 5. (a) Representation of the data-pyramid of a 12 mm wide circular sample of CVD graphene transferred to 90 nm SiO₂ using oxidative decoupling transfer, while (b) is the corresponding data pyramid from coverage analysis. The contrast of images is slightly enhanced to increase visibility. In the left and right sides of figure (c–e) is shown the raw images and digitally detected counterparts, respectively, of selected areas in the data-pyramid highlighted in (a). The dataset is 16·10⁹ (16 giga) RGB pixels.

By examining a specific area more closely, we can highlight the detailed level of the coverage mapping in Fig. 4(c,d). Small holes and lines of missing graphene from the growth and/or transfer process are precisely determined, within the limit of the optical system used. A BLG region around a small three-layer graphene area in the centre of the image (black circle) is also well represented in the coverage map as bilayer graphene and “other”, respectively. The bright blue dots on the sample are polymer residues remaining from the transfer method, also represented as “other” in the coverage map. Based on an optical image, it cannot be excluded that there is graphene beneath areas covered by polymer residue. Therefore, the numerical graphene coverage determined with this method strictly serves as the lower bound for the coverage, or specifically the coverage of SLG without macroscopic contamination. Figure 4(d) clearly shows the regions with SiO₂, SLG, and BLG, as well as regions with everything else marked as black. Figure 4(e) shows the Raman spectroscopic $I(2D)/I(G)$ peak intensity ratio, for comparison with Fig. 4(c,d). It is clearly seen that $I(2D)/I(G)$ is ~ 2 in the areas discerned as SLG in the coverage map, while $I(2D)/I(G)$ drops to ~ 1 for the BLG region inside the black circle, as expected⁴⁷. As the red arrows in Fig. 4(e) indicate, the Raman analysis shows graphene in areas that the quantitative optical method categorises as “other”, which confirms the presence of graphene under macroscopic contaminants. The Raman mapping confirms that the coverage analysis gives a lower bound of the 2D material coverage in cases where the sample is contaminated.

The technique presented here is thus a way to systematically determine not only the presence and number of graphene layers, but also whether it is free from or covered by residues or other contamination, or contains macroscopic defects such as folding and tearing.

Scalable inspection using data-pyramids. Since handling of numerical data and images in the giga-pixel range and beyond is outside the capabilities of most commercially available software and analysis systems, we use here an approach that draws inspiration from online services for presenting geo-spatial data that allows visualization and numerical analysis to be carried out on arbitrarily large data sets with very moderate computing power.

Data pyramids are hierarchical sets of data obtained by progressively subsampling which in the present case have spatial extent. Data pyramids only show and treat data at a resolution that is relevant to the user and the spatial scale at which the data is viewed, rather than the full resolution. This data-structure allows correlation of several data sets with shared coordinates, highly efficient numerical analysis, and handling of essentially arbitrarily large data sets. The bottom level of the pyramid contains full-resolution data while each subsequent level is sampled to half the side-length (and thus a quarter of the resolution), as illustrated in Fig. 5(a,b). Data pyramids are the underlying principle of the smooth, streaming experience in online map services, which supports seamless zooming spanning more than 10 orders of magnitude in scale⁴⁸.

Every move up in the pyramid results in the side-lengths being halved. The total number of levels, l_{max} , is thus given by how many times we can down-sample the longest side of the full-resolution level, given by,

$$l_{max} = \lceil \log_2(\max(x_{max}, y_{max})) \rceil. \quad (2)$$

The total size of the dataset thus increases as levels are added on top of the bottom (full resolution). As each subsequent level in the data-pyramid is one quarter the size of the previous, the maximum possible increase in size of the dataset is given by

$$\frac{1}{4} + \frac{1}{16} + \frac{1}{64} + \dots = \sum_{n=1}^{\infty} \frac{1}{4^n} = \frac{1}{3}. \quad (3)$$

Building a data-pyramid thus increases the total size of the dataset by no more than a factor of 4/3, a modest amount considering that it allows for easy inspection and numerical processing of arbitrarily large datasets. After the data-pyramid has been generated, virtually no processing power is needed to inspect the data, as the (next) required level is simply (pre)loaded into memory.

Given that only a subset of the full data is ever accessed, it is possible to do on-demand real-time processing of the data. Most types of trivial data analysis or image treatment of the accessed data, such as contrast enhancement, statistical analysis, etc., are computationally inexpensive to perform. We present an example of a zoomable map of graphene including on-demand processing options using correlated data pyramids, which can be found online⁴⁹.

The data pyramids are generated from a large number of images collected with an optical microscope with a standard motorised stage. An overlap of ~5% for adjacent images is in most cases sufficient to generate near-seamless, continuous images of arbitrarily high resolution. Each data pyramid is generated by successively down-sampling the images, starting with the full-resolution data, and repeating this process until the final level is 1×1 pixel. This is illustrated in Fig. 5, which shows four successive levels of pyramids for optical and coverage data (Fig. 5(a,b)), as well as images for three representative areas in the highest resolution layer (Fig. 5(c–e)). In principle, the only limit to the size of the data pyramids is data collection and storage, which even with modest desktop solutions can reach tera-pixel resolution and beyond.

Conclusion

In conclusion, we have presented an accurate, robust and fully automatic method for identification of graphene or other 2D materials, which successfully rejects false-positives and false-negatives. The accuracy of the quantitative coverage measurements of graphene has been shown to depend on the degree of contamination, but the method give a reliable lower-bound estimates of the coverage.

The method employs a combination of the RGB spectral fingerprints from all relevant parts of the light path; the light source, the detector, the two-dimensional film and the substrate, and refines the coverage using a combination of well-established image processing methods. Data pyramids are computationally and resource efficient for an arbitrarily large dataset of images, and serve as an optimal platform for quantitative and qualitative analysis of 2D material films on arbitrarily large areas, with a resolution ultimately limited by the microscope optics used. The method can be used for automated identification and analysis of exfoliated materials, which is a tedious and error-prone procedure when performed manually, for in-line quality control of CVD graphene, or as an effective means of monitoring improvements in 2D material transfer and growth methods. Such data sets form a basis for data mining and deep statistical analysis of results generated across long time spans and between disparate characterisation techniques and provide the possibility to extract trends and correlations that would not be apparent from manual inspection of isolated regions alone.

References

1. Blake, P. *et al.* Making graphene visible. *Appl. Phys. Lett.* **91**, 63124 (2007).
2. Gorbachev, R. V. *et al.* Hunting for monolayer boron nitride: Optical and raman signatures. *Small* **7**, 465–468 (2011).
3. Pizzocchero, F. *et al.* Non-destructive electrochemical graphene transfer from reusable thin-film catalysts. *Carbon* **85**, 397–405 (2015).
4. Whelan, P. R. *et al.* Raman spectral indicators of catalyst decoupling for transfer of CVD grown 2D materials. *Carbon* **117**, 75–81 (2017).
5. Wang, R. *et al.* Catalyst interface engineering for improved 2D film lift-off and transfer. *ACS Appl. Mater. Interfaces* **8**, 33072–33082 (2016).
6. Hao, Y. *et al.* The role of surface oxygen in the growth of large single-crystal graphene on copper. *Science* **342**, 720–3 (2013).
7. Mohsin, A. *et al.* Synthesis of millimeter-size hexagon-shaped graphene single crystals on resolidified copper. *ACS Nano* **7**, 8924–8931 (2013).
8. Wang, C. *et al.* Growth of millimeter-size single crystal graphene on Cu foils by circumfluence chemical vapor deposition. *Sci. Rep.* **4**, 4537 (2014).
9. Miseikis, V. *et al.* Rapid CVD growth of millimetre-sized single crystal graphene using a cold-wall reactor. *2D Mater.* **2**, 14006 (2015).
10. Wu, T. *et al.* Fast growth of inch-sized single-crystalline graphene from a controlled single nucleus on Cu–Ni alloys. *Nat. Mater.* **15**, 43–47 (2015).
11. Braeuninger-Weimer, P., Brennan, B., Pollard, A. J. & Hofmann, S. Understanding and controlling Cu catalyzed graphene nucleation: The role of impurities, roughness and oxygen scavenging. *Chem. Mater.* **28**, 8905–8915 (2016).
12. Wang, Y. *et al.* Electrochemical delamination of CVD-grown graphene film: Toward the recyclable use of copper catalyst. *ACS Nano* **5**, 9927–9933 (2011).
13. Gao, L. *et al.* Repeated growth and bubbling transfer of graphene with millimetre-size single-crystal grains using platinum. *Nat. Commun.* **3**, 699 (2012).
14. Bøggild, P. *et al.* Mapping the electrical properties of large-area graphene. *2D Mater.* **4**, 42003 (2017).
15. Buron, J. D. *et al.* Graphene conductance uniformity mapping. *Nano Lett.* **12**, 5074–5081 (2012).
16. Mackenzie, D. M. A. *et al.* Quality assessment of graphene: Continuity, uniformity, and accuracy of mobility measurements. *Nano Res.* **10**, 1–10 (2017).
17. Schriver, M. *et al.* Graphene as a long-term metal oxidation barrier: Worse than nothing. *ACS Nano* **7**, 5763–5768 (2013).
18. Rensink, R. Change detection. *Annu. Rev. Psychol.* **53**, 245–277 (2002).
19. Luo, B. *et al.* Copper oxidation through nucleation sites of chemical vapor deposited graphene. *Chem. Mater.* **28**, 3789–3795 (2016).

20. Li, X. *et al.* Transfer of large-area graphene films for high-performance transparent conductive electrodes. *Nano Lett.* **9**, 4359–4363 (2009).
21. Lee, Y. *et al.* Wafer-scale synthesis and transfer of graphene films. *Nano Lett.* **10**, 490–3 (2010).
22. Novoselov, K. S. *et al.* Electric field effect in atomically thin carbon films. *Science* **306**, 666–669 (2004).
23. Larsen, M. B. B. S., Mackenzie, D. M. A., Caridad, J. M., Bøggild, P. & Booth, T. J. Transfer induced compressive strain in graphene: Evidence from Raman spectroscopic mapping. *Microelectron. Eng.* **121**, 113–117 (2014).
24. Byrnes, S. J. Multilayer optical calculations. *arXiv*, 1603.02720 (2016).
25. Bruna, M. & Borini, S. Assessment of graphene quality by quantitative optical contrast analysis. *J. Phys. D. Appl. Phys.* **42**, 175307 (2009).
26. Ni, Z. H. *et al.* Graphene thickness determination using reflection and contrast spectroscopy. *Nano Lett.* **7**, 2758–2763 (2007).
27. Roddaro, S., Pingue, P., Piazza, V., Pellegrini, V. & Beltram, F. The optical visibility of graphene: Interference colors of ultrathin graphite on SiO₂. *Nano Lett.* **7**, 2707–2710 (2007).
28. Jung, I. *et al.* Simple approach for high-contrast optical imaging and characterization of graphene-based sheets. *Nano Lett.* **7**, 3569–3575 (2007).
29. Weber, J. W., Calado, V. E. & Van De Sanden, M. C. M. Optical constants of graphene measured by spectroscopic ellipsometry. *Appl. Phys. Lett.* **97** (2010).
30. Green, M. A. & Keevers, M. J. Optical properties of intrinsic silicon at 300 K. *Prog. Photovolt.* **3**, 189–192 (1995).
31. Malitson, I. H. Interspecimen comparison of the refractive index of fused silica. *J. Opt. Soc. Am.* **55**, 1205 (1965).
32. Sharpe, L. T., Stockman, A., Jagla, W. & Jägle, H. A luminous efficiency function, $V^*(\lambda)$, for daylight adaptation. *J. Vis.* **5**, 3 (2005).
33. Beal, A. R., Liang, W. Y. & Hughes, H. P. Kramers-Kronig analysis of the reflectivity spectra of 3R-WS₂ and 2H-WSe₂. *J. Phys. C* **89**, 2449 (1976).
34. Zhao, W. *et al.* Evolution of electronic structure in atomically thin sheets of WS₂ and WSe₂. *ACS Nano* **7**, 791–797 (2013).
35. Rubio-Bollinger, G. *et al.* Enhanced visibility of MoS₂, MoSe₂, WSe₂ and black-phosphorus: Making optical identification of 2D semiconductors easier. *Electronics* **4**, 847–856 (2015).
36. Castellanos-Gomez, A., Agrat, N. & Rubio-Bollinger, G. Optical identification of atomically thin dichalcogenide crystals. *Appl. Phys. Lett.* **96** (2010).
37. Çadık, M. Perceptual evaluation of color-to-grayscale image conversions. *Comput. Graph. Forum* **27**, 1745–1754 (2008).
38. Gao, L., Ren, W., Li, F. & Cheng, H.-M. Total color difference for rapid and accurate identification of graphene. *ACS Nano* **2**, 1625–1633 (2008).
39. Chen, Y. F. *et al.* Rapid determination of the thickness of graphene using the ratio of color difference. *J. Phys. Chem. C* **115**, 6690–6693 (2011).
40. Nolen, C. M., Denina, G., Teweldebrhan, D., Bhanu, B. & Balandin, A. A. High-throughput large-area automated identification and quality control of graphene and few-layer graphene films. *ACS Nano* **5**, 914–922 (2011).
41. Abd Rahman, S. F., Hashim, A. M. & Kasai, S. Identification of graphene layer numbers from color combination contrast image for wide-area characterization. *Jpn. J. Appl. Phys.* **51** (2012).
42. Wang, H.-C. *et al.* Large-area few-layered graphene film determination by multispectral imaging microscopy. *Nanoscale* **7**, 9033–9039 (2015).
43. Ataman, E., Aatre, V. & Wong, K. Some statistical properties of median filters. *IEEE Trans. Acoust.* **29**, 1073–1075 (1981).
44. Bovik, A. C., Huang, T. S. & Munson, D. C. The effect of median filtering on edge estimation and detection. *IEEE Trans. Pattern Anal. Mach. Intell.* **PAMI-9**, 181–194 (1987).
45. Serra, J. *Image analysis and mathematical morphology*, v.1. (Academic Press, 1982).
46. Suzuki, S. & Abe, K. Topological structural analysis of digitized binary images by border following. *Comput. Vision, Graph. Image Process.* **30**, 32–46 (1985).
47. Reina, A. *et al.* Large area, few-layer graphene films on arbitrary substrates by chemical vapor deposition. *Nano Lett.* **9**, 30–35 (2009).
48. Rosenfeld, A. *Multiresolution image processing and analysis*. (Springer Science & Business Media, 2013).
49. Jessen, B. S. & Whelan, P. R. Quantitative optical map of graphene. Available at: <http://tinyurl.com/DTU-GMAP> (2017).

Acknowledgements

B.S.J. and P.B. thank the Danish National Research Foundation Centre for Nanostructured graphene, DNRF103, and EU Horizon 2020 ‘Graphene Flagship’ 696656. P.R.W. and P.B. acknowledge financial support from Innovation Fund Denmark DA-GATE 0603-005668B. P.R.W., B.L., J.D.T. and T.J.B. acknowledge financial support from EU FP7-604000 GLADIATOR. D.M.A.M. acknowledges Villum Fonden project no. VKR023117 and EC Graphene FET Flagship contract number 604391.

Author Contributions

B.S.J. and P.R.W. conceived the project and developed the method. P.R.W. and B.L. grew and transferred CVD samples, while B.S.J., J.D.T. and L.G. prepared samples of exfoliated crystals. Raman spectroscopy and analysis was performed by D.M.A.M. The work was supervised by T.J.B. and P.B. All authors contributed to the preparation of the manuscript.

Additional Information

Supplementary information accompanies this paper at <https://doi.org/10.1038/s41598-018-23922-1>.

Competing Interests: The authors declare no competing interests.

Publisher's note: Springer Nature remains neutral with regard to jurisdictional claims in published maps and institutional affiliations.



Open Access This article is licensed under a Creative Commons Attribution 4.0 International License, which permits use, sharing, adaptation, distribution and reproduction in any medium or format, as long as you give appropriate credit to the original author(s) and the source, provide a link to the Creative Commons license, and indicate if changes were made. The images or other third party material in this article are included in the article's Creative Commons license, unless indicated otherwise in a credit line to the material. If material is not included in the article's Creative Commons license and your intended use is not permitted by statutory regulation or exceeds the permitted use, you will need to obtain permission directly from the copyright holder. To view a copy of this license, visit <http://creativecommons.org/licenses/by/4.0/>.

© The Author(s) 2018